PHYSICAL REVIEW B **99**, 035417 (2019)

Broadband light-trapping enhancement of graphene absorptivity

Xiwen Zhang and Sajeev John[*]
Department of Physics and Astronomy, University of Toronto, 60 Saint George Street, Toronto, Ontario, Canada M5S 1A7

(Received 2 October 2018; revised manuscript received 15 November 2018; published 9 January 2019)

Low optical absorptivity of graphene limits the quantum efficiency of graphene-based optoelectronic devices. We demonstrate a broadband enhancement of absorptivity in an architecture of graphene intercalation inside a simple-cubic woodpile photonic crystal. Significant light-trapping effect is achieved due to spectrally broad and dense resonances in the architecture, especially modes propagating nearly parallel to the interface between the photonic crystal and the background material. We demonstrate an overall absorptivity ∼10 to 17 times larger than the free-standing bare graphene monolayer with bandwidth to central frequency ratio 0.3, and ∼5 to 11 times larger with bandwidth to central frequency ratio 1.33. A distributed intercalation of three graphene monolayers proves a ∼70% overall absorptivity with bandwidth to central frequency ratio 0.3.

DOI: 10.1103/PhysRevB.99.035417

I. INTRODUCTION

The unique physical properties of graphene have attracted broad interest in fundamental science and technological applications. Both electrons and holes in graphene are Dirac fermions with vanishing effective mass, giving rise to an extraordinarily high electron mobility ($\sim 2 \times 10^5\ \mathrm{cm^2\,V^{-1}\,s^{-1}}$ at electron density $\sim 2 \times 10^{11}\ \mathrm{cm^{-2}}$) [1–3]. As a monolayer of carbon atoms, graphene absorbs ∼2% of the incident light over a broad spectrum from the far infrared all the way to the ultraviolet [4–6]. These transport and optical properties, together with its excellent thermal [7] and mechanical characteristics [8], make graphene a promising and unique candidate material for ultrafast and ultrabroadband optoelectronic devices with low energy consumption, low fabrication costs, and small device footprint [9–13], such as ultrafast lasers [14,15], optical modulators [16–20], and transparent electrodes [21] in photovoltaic devices [22,23]. Numerous studies have focused on the development of graphene-based photodetectors [24–31], which in principle can operate over a bandwidth much broader than traditional detectors.

However, graphene has very short-lived (approximately a picosecond) photogenerated carriers [32], making it difficult to form a photocurrent. Also, graphene has a very small optical thickness despite its large absorption coefficient, which strongly limits its photodetection capability. Various methods are used to overcome the first drawback, such as imposing external or internal electric fields [25,33] and creating a potential barrier between two graphene layers to reduce hot carrier recombination [29]. In this work we present a broadband mechanism for enhancing photocarrier generation in graphene through light trapping in a suitably designed photonic crystal (PC).

In the last decade, numerous schemes have been suggested and demonstrated to increase the light-harvesting efficiency of graphene. One method is to strongly localize incident light to graphene through plasmon excitation. There are two ways of doing this. The first one is to lay graphene sheets adjacent to gold nanoparticles [26], a nanograting [34], or nanoantennas [35], using the near-field enhancement due to the excitation of metallic surface plasmons on these gold nanostructures. Such methods work in the visible and near-infrared regime, but introduces energy loss in the metals [36–38]. With suitable design of the nanostructures [35], some of the hot electrons that surface plasmons decay into can be transferred from gold to graphene, acting as a plasmon-induced doping [39] and contributing to the photocurrent. The carrier mobility with gold nanoparticles on substrate-supported graphene was $\sim 10^3\ \mathrm{cm^2\,V^{-1}\,s^{-1}}$ [26].

The second way of introducing plasmon resonances is to dope the graphene. This enhances absorptivity in the mid- to far-infrared region, where intraband transition dominates the graphene conductance [40]. A periodic array of graphene nanodisks, ribbons, or other structures can provide graphene plasmon resonances to boost light absorptivity [41–46]. However, this breakup of the graphene sheet degrades carrier mobility. Alternatively, the doped graphene plasmon resonance can be excited by dielectric [47–50] and metallic [51,52] grating couplers, leaving the doped graphene layers intact. These methods are tuned to work only in the infrared frequency range determined by the nature of graphene plasmon resonance.

Another method is to place graphene on a waveguide to increase the local field strength. High-responsivity graphene photodetectors [28,53,54] and optical modulators [16] were experimentally demonstrated using silicon waveguides. These devices are polarization and mode selective, operating within the frequency range limited by the silicon band gap ∼1.1 eV. The optical coupler needed to feed light into the waveguide may introduce significant amount of loss [53]. A one-dimensional PC waveguide made of holes etched in a silicon nanobeam was proposed to achieve near-infrared narrow-band perfect absorption of a graphene/$\mathrm{Al_2O_3}$ multilayer stack filled into these PC holes [55]. However, it is difficult to extract the photogenerated carriers in such a configuration.

---

[*] john@physics.utoronto.ca

Apart from the above, a Fabry-Pérot microcavity [56], two-dimensional PC defect cavities [57,58] and dielectric gratings [59–64] were integrated with graphene to achieve high absorption but only at specific frequencies. Graphene-covered metal gratings [65–67] were suggested to excite magnetic polaritons to improve graphene's near-infrared absorptivity, but is accompanied by energy loss in the metal. Ray-trapping configurations [68–70], where destructive interference in reflection and total internal reflection confine incident light of a specific input angle to the position of graphene, achieved broadband absorption enhancement, but only at critical angles.

A PC is another way of achieving strong localization of light [71]. One-dimensional multilayer PCs have been suggested to enhance the graphene absorptivity using a surface defect mode [72], a PC-localized mode [73], and guided modes [74,75]. These schemes target absorptivity enhancement in a small frequency range. Two-dimensional PCs composed of a square lattice of air holes in a dielectric slab were used for light harvesting in nearby graphene [76,77] under the critical coupling with the PC guided resonances [78]. In general, the sparse distribution of resonant light-trapping modes limits the overall performance of the light harvesting in graphene integrated in one- and two-dimensional PCs.

An improved scheme of increasing graphene light absorptivity for ultrabroad and ultrafast photodetection should cover a large bandwidth without parasitic losses, while retaining the high mobility of photogenerated carriers. In this paper we discuss a broadband absorptivity enhancement scheme based on a three-dimensional (3D) simple-cubic woodpile PC made of TiO_2. This enhancement occurs within the higher-order bands of the PC at frequencies above the fundamental stop gaps of the photonic band structure. This spectral region is characterized by an enhancement of the overall photonic density of states beyond that of a homogeneous medium.

The advantage of this 3D PC with simple cubic symmetry lies in a broad and dense continuum of resonant modes spanning a large frequency range [79]. This enables full utilization of undoped graphene's broad, flat absorption spectrum, with the upper limit imposed by the band gap of TiO_2, which is $\sim$3 eV [80–82]. Among these resonant modes, we are particularly interested in the parallel-to-interface refractive (PIR) modes [79,83–85] wherein light incident at nearly normal incidence is refracted into PC modes propagating nearly parallel to the air-PC interface. There are unique and favorable properties of PIR modes in light trapping and harvesting. Typical PIR modes have a long lifetime and slow group velocity inside the PC. This increases the interaction time between light and graphene. Moreover, PIR modes have group velocity vectors along the PC material interface and strong spatial overlap with graphene layer placement. This increases the light-graphene interaction length. Overall, the light absorptivity can be greatly enhanced in a large spectral range by intercalating graphene sheets between woodpile layers. Recently, PIR modes in 3D PC have been experimentally shown to greatly enhance the volume absorptivity of light below the electronic band gap of a TiO_2-based PC [86]. In this work, PIR modes were excited directly from normal incident light without requiring a coupler as some other methods do. As we show below, exact normal incidence is not required for large absorption enhancement in our light-harvesting scheme. Also, the absorption enhancement is almost independent on the incident polarization.

In our graphene intercalated woodpile structure the PC lattice supplies transverse momentum to the incoming light, feeding photons into PIR modes along the graphene. Using the configurations of two-layer and six-layer woodpiles placed on top of a perfect reflector, we demonstrate graphene monolayer overall absorptivities of 21.8% and 31.4% (with peak absorptivities of 99.9% and 98.6%), respectively, with bandwidth to central frequency ratio 0.3. Increasing the number of graphene monolayers to three in the six-layer woodpile configuration raises the absorptivity to 69.6%. The light-harvesting bandwidth can be further increased by extending to higher-order resonance modes. Considering the small thickness of the graphene, our scheme may in turn provide a potential way of field-distribution tomography inside PC.

II. BARE GRAPHENE ABSORPTIVITY

Graphene is a semimetal with a honeycomb lattice consisting of two sublattices that can be described mathematically in terms of pseudospins at the Dirac point [87,88]. Its optical conductivity can be obtained using the Kubo formula for the effective pseudospin-form Hamiltonian [88–90]. For the sake of simplicity and scalability (in frequency), we work at zero temperature and assume that the Fermi surface lies near the Dirac point, so that only the interband transition contributes to the conductivity. These result in a constant optical conductivity $\sigma = e^2/(4\hbar)$, where e is the single electron charge. Under the normal incidence of light, the transmissivity (T), reflectivity (R), and absorptivity (A) of a free-standing bare graphene monolayer in air [91] are $T = (1+\pi\alpha/2)^{-2} \approx 97.75\%$, $R = (\pi\alpha/2)^2 T \approx 0.01\%$, and $A \approx \pi\alpha \approx 2.24\%$, respectively, where $\alpha = [1/(4\pi\varepsilon_0)](e^2/\hbar c)$ is the fine structure constant in SI unit, and ε_0 is the vacuum permittivity.

The graphene optical absorptivities with and without PC enhancement are simulated by solving Maxwell's equation via the finite-difference time-domain (FDTD) method [92]. Depending on the specific size of the PC unit cell, there may be a significant mismatch between the size of the light-trapping architecture and thickness d of the graphene. For computational simplicity, we model the graphene layer as a finite thickness absorber. The thickness d is chosen to be small enough not to disturb the modes of PC, while large enough to be discernible with the resolution of the FDTD mesh. In order to render a general frequency scaling of the absorptivity spectrum, we choose $d = a/45$ (where a is the size of the PC unit cell) to also be the resolution of the mesh grid of the numerical simulation. Since the wavelengths λ we focus on are in the range of a–$2a$, the graphene region thickness d is between $\lambda/90$ and $\lambda/45$. This does not perturb the resonant modes of our PC.

To model graphene as an absorptive dielectric, we write its dielectric constant $\varepsilon_r = \varepsilon_r' + i\varepsilon_r''$, where ε_r' and ε_r'' are real and imaginary parts, respectively. The imaginary part of the dielectric constant is related to the conductivity $\varepsilon_r'' = e^2/(4\varepsilon_0\hbar\omega d) = \alpha\lambda/(2d)$ and the real part is set to $\varepsilon_r' = 1$, where $d = a/45$, α is the fine structure constant, and λ is the input optical wavelength in vacuum. Numerically, the effective dielectric constants of the absorber and its immediate environment are assigned by the FDTD algorithm [93]. This may be affected by the choice of d and the mesh resolution. For both $d = a/45$ and $d = a/75$ (with resolution equal to d) the average real parts of the effective dielectric constant (assigned by our FDTD algorithm) are 1.33 for the absorber itself and 2.5 for its immediate environment.

A useful parameter for understanding the light trapping in graphene is its absorption quality factor Q_{abs} [79], which is defined as the product of the central frequency of the input light and the time τ_{abs} it takes the light to decay to $1/e$ of its initial amplitude in the absorber (see Sec. III). Q_{abs} is essentially determined by the real and imaginary parts of the dielectric constant. We bear in mind in our model that the absorption timescale in the graphene layer can be affected if the thickness d is chosen unrealistically.

III. GRAPHENE INTERCALATION WITHIN A SIMPLE-CUBIC WOODPILE PHOTONIC CRYSTAL

The 2.24% fraction of light absorption in a graphene monolayer is too small for many optoelectronic devices. One way to improve the absorptivity of graphene is to manipulate the Fermi energy by doping with impurities or applying gate voltages [94], etc. Independently of the material's electronic properties, a more effective enhancement of light harvesting is realized by localizing the incident optical field near the position of the graphene. We achieve this via a dense continuum of resonant optical Bloch modes of a simple cubic PC that naturally fits the broad and flat absorption spectrum of graphene.

Our architecture is shown in Fig. 1. It consists of a simple cubic TiO_2 woodpile, six layers in height, infinite in the transverse direction x-y, and resting on a solid substrate. Each woodpile log, with refractive index 2.25, has width of w and height of $h = a/2$, where a is the simple cubic lattice constant. In order to isolate the graphene absorption enhancement, absorption in TiO_2 is neglected. The filling factor, determined by the woodpile width w, is taken to be 0.5. The woodpile layer is labeled with a number starting from 1 denoting the very top layer. In the presence of graphene, the whole structure is denoted as n-g-m, where n and m are the number of log layers above and below the graphene layer, respectively. For instance, Fig. 1(a) corresponds to 2-g-4.

The nonabsorbing substrate of the structure is taken to be either fused silica (FS) with refractive index 1.46 or a perfect mirror (MR). The background material is air with refractive index of unity. The frequency is scaled in unit of c/a Hz, where c is the speed of light in vacuum. This corresponds to the dimensionless quantity a/λ, where λ is the vacuum wavelength. For example, for a woodpile PC with unit cell size $a = 450$ nm, frequency 1 c/a corresponds to 666 THz and wavelength 450 nm. In this work we mainly consider normally incident light with x-polarized electric field unless otherwise specified.

We define a bandwidth dependent overall absorptivity enhancement as follows:

$$\beta = \int_{f_1}^{f_2} df\, A(f) \Big/ \int_{f_1}^{f_2} df\, A'(f), \tag{1}$$

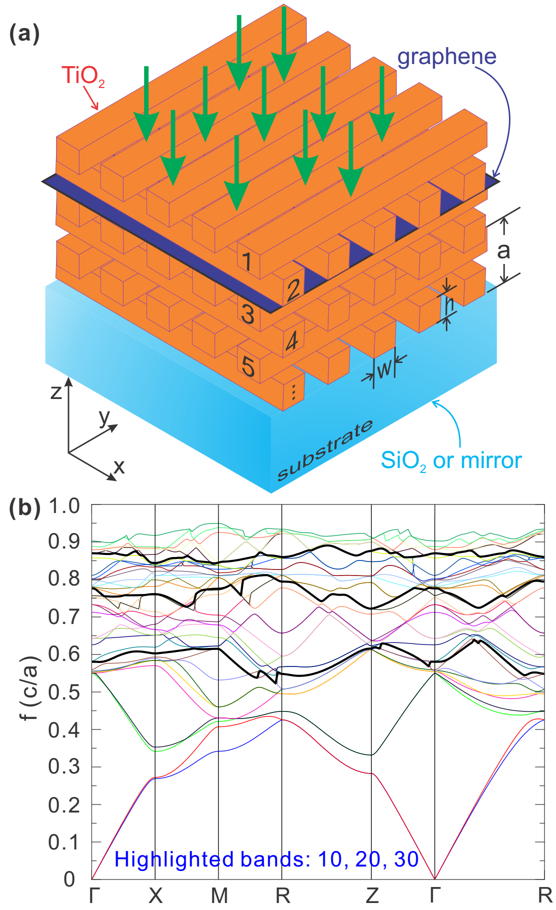

FIG. 1. Illustration of graphene absorption enhancement scheme. (a) A graphene layer is inserted into a 3D simple cubic PC. (b) The band diagram for a TiO_2 woodpile PC in air background with filling factor 0.5 and refractive index $n = 2.25$.

where f_1 and f_2 are the lower and upper frequency bounds, A is the graphene absorptivity in our light-trapping architecture, and A' is the absorptivity of the free-standing bare graphene monolayer.

We consider a PC with 3 unit cells (6 layers of woodpile) in height. Inserting a graphene layer just below the first unit cell (counting from the top), the architecture is depicted in Fig. 1(a). We first compare the transmissivity, reflectivity and absorptivity without and with graphene layer.

For a PC with 3 unit cell along z, Fig. 2(a) reveals a range of broad, high transmissivity peaks from a continuum of resonant modes inside the PC that may assist in enhancement of graphene absorption. Indeed, Fig. 2(b) shows that over the frequency range from 0.55 to 0.85 c/a, overall absorption enhancement (relative to a free-standing graphene monolayer) is 9.42, while in the region that from 0.55 to 0.75 c/a, the overall enhancement factor is 10.73.

The high transmissivity spectrum also exhibits some narrow dips, especially in the lower band region (within the scope of the tenth photonic band). They are located at $f = 0.5635$, 0.5822, and 0.6018 c/a in Fig. 2(a). Since there is no band gap in this frequency range [as seen from Fig. 2(c)], these strong reflection peaks may indicate the existence of high quality factor resonances with field localized in the PC. This

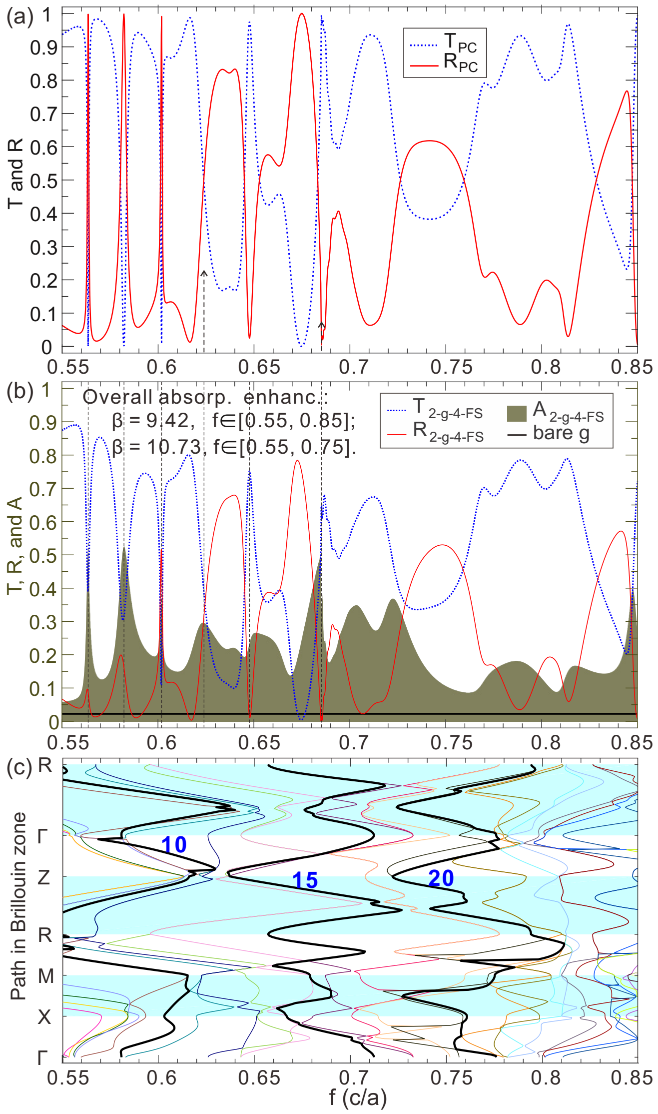

FIG. 2. Transmissivity, reflectivity, and absorptivity (a) without and (b) with graphene in a 3-unit-cell woodpile PC on a fused silica substrate. (a) Transmissivity (dotted blue line) and reflectivity (solid red line) with normal incident light shining from above the PC. (b) The reflectivity (red solid line) and absorptivity (brown filled color) of the same setup as in (a) except now with a graphene monolayer placed below the second woodpile layer (2-g-4 configuration in our notation). For comparison and visualization, the absorptivity of a free-standing bare graphene monolayer is plotted in the same figure with solid black line, and the band diagram of the same type of woodpile PC (infinite size in all three dimensions) is presented in (c). The 10th, 15th, and 20th photonic bands are highlighted in (c) to locate the absorption peaks in terms of PC bands, and some vertical dashed lines are drawn in (b) to guide the view for a comparison with the transmissivity and reflectivity of the PC in (a).

is confirmed by the absorption profile of the graphene layer in Fig. 2(b) at these frequencies: the strong absorption peaks when the graphene lies in the upper part of the PC show that these modes are strongly excited.

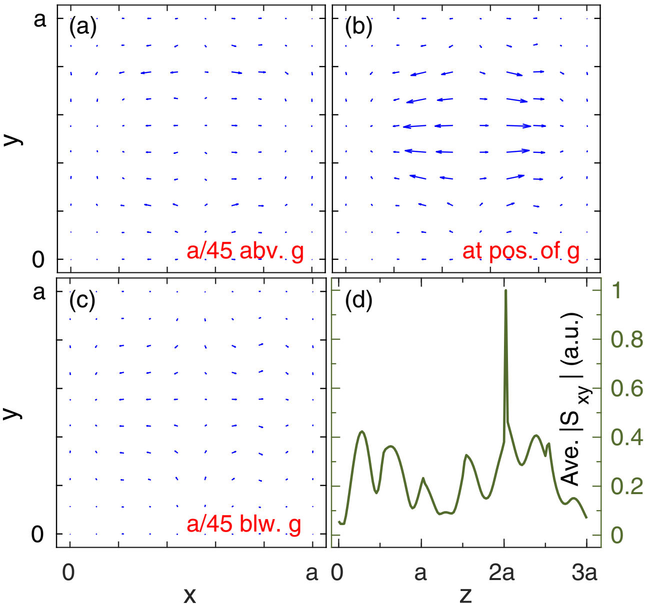

FIG. 3. Distribution of the transverse Poynting vectors S_{xy} as a function of vertical location z for the PC resonant mode at $f = 0.5825\ c/a$ in the 2-g-4 configuration. (a)–(c) A distribution of transverse Poynting vectors at locations of $a/45$ above graphene, at the graphene monolayer, and $a/45$ below graphene, respectively. To clearly see the Poynting vectors, we disregard the graphene while keeping the vacancy space at the location of the graphene. (d) Averaged transverse Poynting vector magnitude $\overline{S_{xy}}$ as a function of longitudinal position z, with $z = 0$ referring to the bottom of the PC (touching the substrate), and $z = 3a$ the top of the PC structure.

For further investigation, we focus on the second absorption peak (counting from the left) in Fig. 2(b) at frequency $0.5822\ c/a$. In Fig. 3 we plot the transverse components of Poynting vector **S** at this frequency as a function of z. It is readily seen from Figs. 3(a)–3(c) that a transversely propagating mode(s) quickly develops near the location between the bottom of the second woodpile layer and top of the third woodpile layer (counting from the top). This is a PIR resonance mode, which propagates with slow group velocity along the woodpile logs and exhibits a long lifetime. To see the spatial distribution of this mode, it is convenient to introduce an averaged transverse Poynting vector magnitude:

$$\overline{S_{xy}}(z) \equiv \iint_{a^2} dxdy\sqrt{S_x(x,y,z)^2 + S_y(x,y,z)^2}, \qquad (2)$$

where the integral is performed over the transverse area of a unit PC cell, and $S_{x,y,z}$ denotes the x, y, and z components of the Poynting vector. This averaged transverse Poynting vector magnitude is an indicator of how strong a transversely propagating mode is excited as a function of z. Figure 3(d) shows that the resonance near $f = 0.5825\ c/a$ has largest parallel-to-interface flow between the second and third woodpile in the 3-unit-cell PC.

In Fig. 4 we plot spectra for the remaining six possible graphene placements inside the six-layer TiO_2 woodpile. At different locations in the PC, the graphene absorption peaks shift, indicating different modes with different spatial distributions. The heights of these absorption peaks also vary from location to location. Some understanding of the amount of absorption follows from mode-coupling theory [79] which suggests that absorption optimization occurs when the dwell

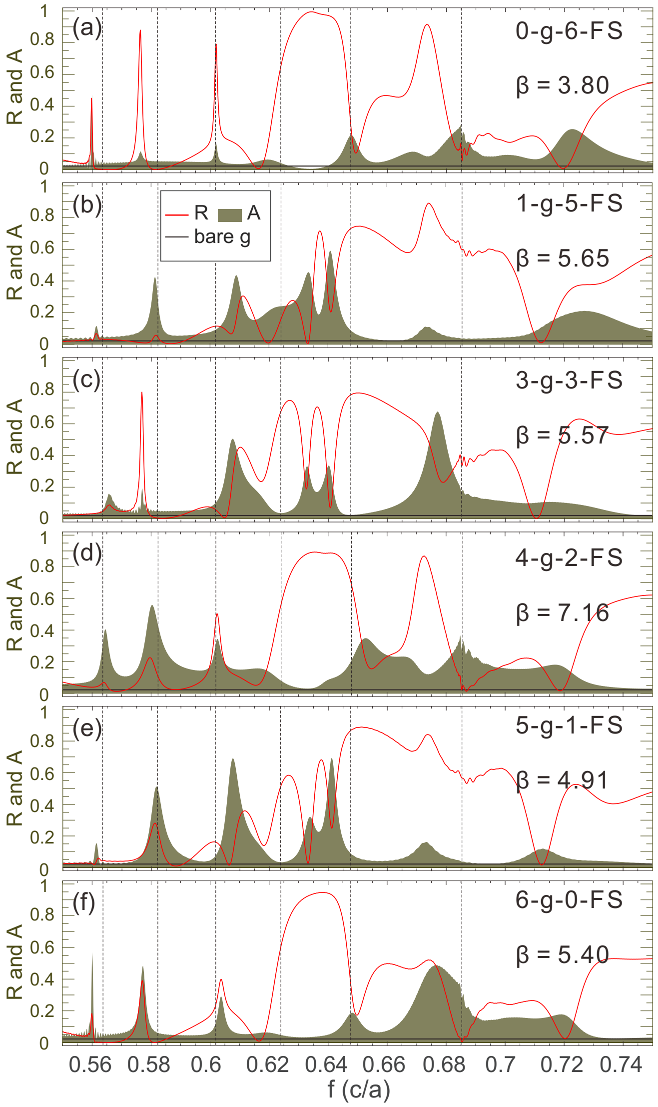

FIG. 4. Absorption and reflection spectrum of a graphene layer placed at different locations of a 3-unit-cell PC: Configurations (a) 0-g-6, (b) 1-g-5, (c) 3-g-3, (d) 4-g-2, (e) 5-g-1, and (f) 6-g-0. Dashed lines mark the same frequencies as in Fig. 2.

time of light in the cavity matches the absorption timescale. This can also be expressed as the mode quality factor Q_{cav} matching the graphene absorption quality factor Q_{abs} [79]. In a resonator with open transmission, reflection, and absorption channels, mode-coupling theory predicts a maximum absorptivity of 50%. This is qualitatively seen in the absorption peak at 0.5822 c/a in Fig. 2(b). However, the mode-coupling analysis [79] is strictly valid in the case of a single mode, and only provides generally trends in a complex multimode situation such as ours. The resonant modes in our PC have substantially different Q factors depending on the locations. This partially appears in the variation of peak absorption with location for the same frequency in Fig. 4. By comparing Figs. 2(b) and 4, it is seen that placing the graphene in between the second and third woodpile layers leads to the largest overall light absorption by the graphene in the frequency range from 0.55 to 0.75 c/a, when using a fused silica substrate.

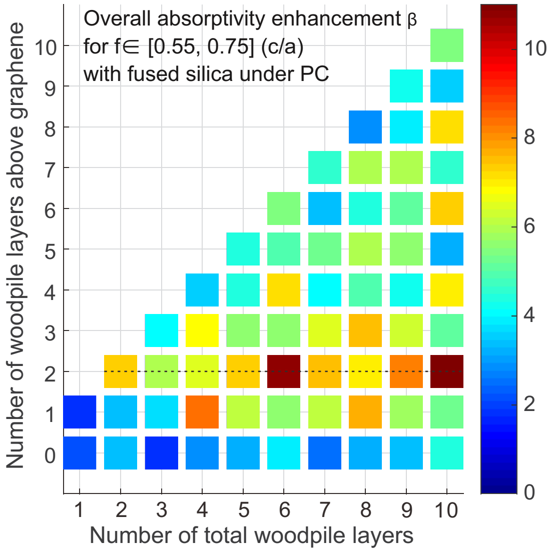

FIG. 5. Overall absorptivity enhancement in frequency range 0.55 to 0.75 c/a by placing graphene at different locations of PCs with different number of woodpile layers, using fused silica as the substrate. The dashed line shows the optimal position for placing the graphene.

In general, the best absorption enhancement occurs by placing the graphene layer in the upper part of the PC, where PIR resonances are easily accessed and excited. The number of woodpile layers of the PC can also be optimized to support modes with Q factor commensurate with the intrinsic absorptivity of graphene. We simulate all the possible locations to insert graphene for PCs consisting of 1–12 woodpile layers. The overall absorption enhancement in the frequency range of 0.55 to 0.75 c/a is presented in Fig. 5. This again shows that the optimal location of graphene is close to two woodpile layers (one unit cell) from the top in the case of a transmitting fused silica substrate.

Mode-coupling theory [79] also suggests that peak absorption can be increased from 50% to 100% if the transmission channel is eliminated. This is examined in the geometry of Sec. IV, where the fused silica substrate is replaced with a perfectly reflecting mirror.

Although we primarily illustrate trapping x-polarized normal incident light, comparable absorption enhancement occurs for off-normal incidence and other polarizations. Figure 6(a) shows that change of the polarization angle $\theta_{\mathrm{pol}} = \arctan(E_y/E_x)$ (where $E_{x,y}$ are the x and y components of the incident electric field), in the 2-g-4 configuration at normal incidence, leads to overall absorptivity enhancement changes of only 0.7% and 0.4% in the frequency ranges of [0.55, 0.75] c/a and [0.55,0.85] c/a, respectively. Figure 6(b) shows absorption spectra for five incident angles $\theta_{\mathrm{in}} = 0^\circ$, 3° 6°, 9°, and 12°, where 0° refers to the normal incidence. The overall absorptivity enhancement under the four oblique incidences in the frequency range [0.5, 0.8] c/a are 1, 0.99, 0.96, and 0.94 times of that under the normal incidence, respectively. Off-normal incident light may excite modes that are not available under the normal incidence due to phase-matching conditions [86]. Due to the densely distributed resonant modes, the

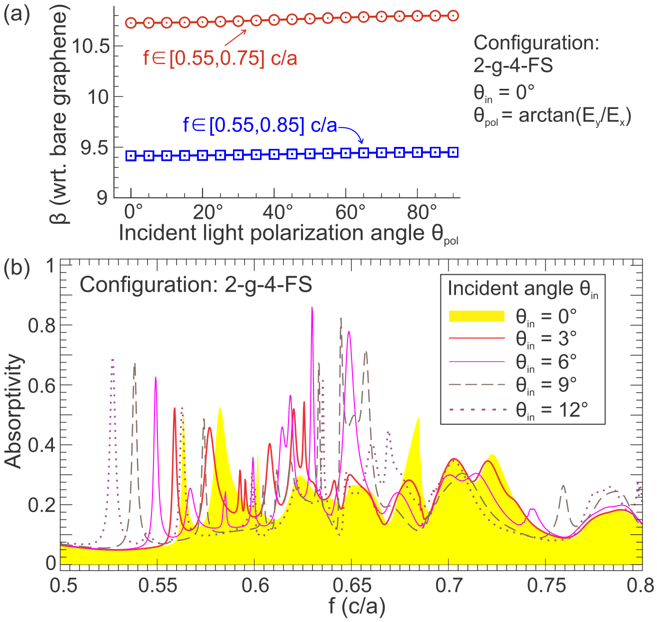

FIG. 6. Incident polarization and angle dependencies of the absorptivity in the 2-g-4 configuration. (a) The overall absorption enhancement β with respect to the bare graphene monolayer as a function of the incident light polarization angle θ_{pol} at normal incidence. The red curve is the overall absorption enhancement in the frequency range of [0.55, 0.75] c/a, and the blue curve is that in the frequency range of [0.55, 0.85] c/a. (b) The absorption spectra under incident angles of 0°, 3°, 6°, 9°, and 12°.

overall absorption enhancement varies only slightly with incident angle.

IV. GRAPHENE EMBEDDED IN PHOTONIC CRYSTAL WITH MIRROR BENEATH

As discussed in Sec. III, the absorptivity can be roughly 50% if the quality factors of the cavity and the absorber match each other. This is evident in Fig. 2(b) at frequency 0.5822 c/a when the peak absorptivity is 52.5%. In this case, a mirror that completely closes the transmission channel may increase the absorptivity to nearly 100%. A signature of such mode-coupling behavior is shown in Fig. 7.

As seen from Fig. 7(c), replacing the substrate of fused silica by a perfect reflector shifts the PIR mode at $f = 0.5822\ c/a$ to $f = 0.5918\ c/a$, and increases the absorptivity peak value to 95.52% as suggested by the mode-coupling theory. The mirror also produces a number of new resonance absorption peaks.

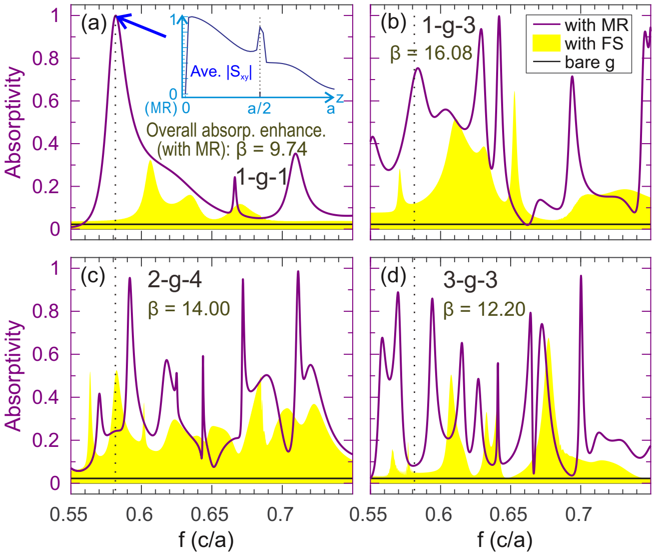

FIG. 7. Absorptivity of graphene embedded in various locations in different PCs with substrates of mirror (purple solid line) and fused silica (yellow filled color). The absorptivity of a free-standing bare graphene monolayer (black solid line) is also plotted for comparison. Dotted lines mark the frequency of the peak absorptivity of (a). The inset in (a) shows the averaged transverse Poynting vector magnitude $\overline{S_{xy}}$, as a function of z, of the mode(s) at the marked frequency. The overall absorptivity enhancement β in the PC with mirror beneath relative to a free-standing graphene monolayer is given in each case. The configurations of graphene and woodpile are (a) 1-g-1, (b) 1-g-3, (c) 2-g-4, and (d) 3-g-3. With a fused silica substrate, the overall absorptivity enhancement in the plotted frequency range (0.55–0.75 c/a) are (a) 3.40, (b) 8.32, (c) 10.73, and (d) 5.57. With the mirror under the PC, the graphene absorptivity is further enhanced (relative to the fused silica substrate) by a factor of (a) 2.86, (b) 1.93, (c) 1.30, and (d) 2.19.

Figure 7(a) reveals that by sandwiching a graphene monolayer between just two woodpile layers and placing a mirror under the whole structure, the absorption peak reaches 99.93% at frequency $f = 0.5817\ c/a$. A detailed examination of the resonant modes at this frequency shows that the averaged transverse Poynting vector magnitude indeed peaks at the position of graphene layer [inset of Fig. 7(a)]. The inset of Fig. 7(a) also shows that the transverse components of the Poynting vector become larger when approaching the mirror. At the surface of the mirror, the tangential components of the electric field and the normal component of the magnetic field must vanish to satisfy the boundary condition of Maxwell's equation. However, surface charges and surface current enable the normal component of electric field and tangential components of magnetic field to be nonzero. As a result, the Poynting vector $\mathbf{S} = \mathbf{E} \times \mathbf{H}$ must lie parallel to the mirror surface. This results in additional long-lived resonance modes near the mirror, with characteristics similar to PIR modes. This synergy between the PIR effect and the backreflector strengthens and enlarges the absorptivity spectrum when the graphene is placed near the bottom of the PC, roughly a half unit cell distance above the mirror.

In Fig. 8 we plot the overall absorptivity enhancement for different graphene positions and various number of woodpile layers in the frequency range from 0.55 to 0.75 c/a. It is seen that placing graphene either near the bottom or top of the PC provides absorptivity enhancement in the presence of perfectly reflecting substrate.

V. INTERCALATION OF MULTIPLE GRAPHENE LAYERS

A way of improving overall absorptivity in graphene-based optoelectronic devices is to simply intercalate numerous graphene layers in the architecture [37,38,43,55,56,68,70,72,73]. For frequency larger than the

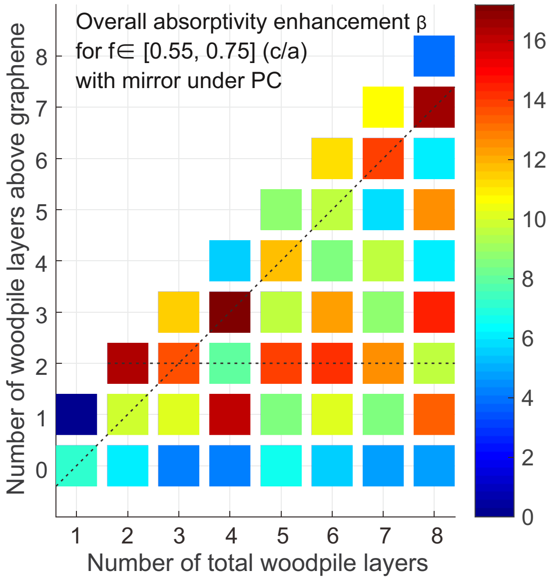

FIG. 8. Overall absorptivity enhancement in frequency range 0.55 to 0.75 c/a by placing graphene at different locations of PC with different numbers of woodpile layers, using a perfect mirror as the substrate. The dashed lines mark the two sets of locations for graphene intercalation leading to the largest absorptivity enhancements.

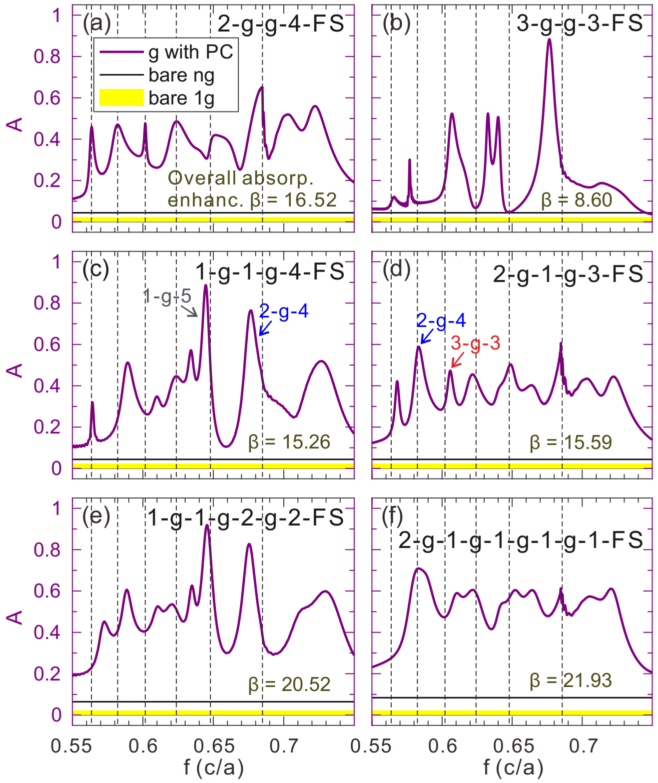

FIG. 9. Absorptivity spectra (solid purple lines) of multiple graphene layers embedded in PC on a fused silica substrate. For comparison, the free-standing bare graphene monolayer absorptivity 2.242% (yellow filled color) and bare graphene multilayer absorptivity (solid black lines) are also plotted. In the latter case, the number of graphene layers is the same as the number of total graphene layers embedded in the PC. The overall enhancement factor β is specified with respect to the graphene monolayer absorptivity. Vertical dashed lines mark the frequencies corresponding to Fig. 2. The arrows in (c) and (d) mark the absorption peaks also observed in configurations 1-g-5, 2-g-4, and 3-g-3.

interlayer electron hopping amplitude, typically in the visible to near infrared regime, a graphene bilayer exhibits optical conductivity roughly twice of that of a graphene monolayer [95–97]. In our simulation we simply increase the imaginary part of the dielectric constant using the same absorber thickness to treat graphene bilayers [in Figs. 9(a) and 9(b)].

In Fig. 9 we show multiple graphene layers absorption spectra in a 3-unit-cell PC. In Fig. 9(a) we consider a graphene bilayer inserted between the second and third woodpile of a 3-unit-cell PC. The overall absorptivity enhancement (compared to a free-standing graphene monolayer) is 16.52. This is also 1.54 times that of a graphene monolayer embedded in the same location of the PC. This location has strongest excited resonant modes for the case of a fused silica substrate. Figure 9(b) shows that it is also possible to boost some specific absorption peaks to very high values by using a graphene bilayer in the 3-g-g-3 configuration.

The graphene bilayer yields an absorption quality factor roughly half that of a monolayers. As discussed in Sec III, this can bring some absorption peaks closer to their optimum while moving others further away. For example, the peak value of the second absorption peak in Fig. 9(a) is 52.5% in the graphene monolayer case [see Fig. 2(b)], whereas it is reduced to 47.05% for the graphene bilayer. Meanwhile, other absorption peaks are increased by replacing a monolayer with a bilayer. For instance, the fourth absorption peak at frequency $f = 0.6242$ c/a is enhanced from 29.58% to 48.62%. The overall absorption is determined by how all the resonance mode lifetimes are matched with graphene absorption timescales on average.

A further opportunity with the graphene-intercalated 3D woodpile is that graphene layers and bilayers can be distributed judiciously throughout the PC. This takes advantage of the spatial distribution of the PC resonance modes to cumulate the different absorption spectra. Figures 9(c) and 9(d) give distinct examples of highly nonuniformly distributed absorption and roughly uniform absorption (with the same overall absorptivity) by embedding two graphene monolayers in different locations of the same PC. Comparing these two figures with Fig. 2(b) and Figs. 4(b) and 4(c), the 1-g-1-g-4 configuration appears to combine the absorption features from 1-g-5 and 2-g-4 configurations [as shown by arrows in Fig. 9(c)]. Similarly, the 2-g-1-g-3 configuration combines the absorption peaks of 2-g-4 and 3-g-3 [as indicated by arrows in Fig. 9(d)]. Spatially separated resonance modes make it possible to raise overall light absorption using distributed graphene layers [for example, Fig. 9(d) vs 9(b)] while keeping features of each monolayer's absorption spectrum. In Figs. 9(e) and 9(f) we insert more layers of graphene to reach even higher overall absorptivity enhancement.

Replacing the substrate of fused silica by a perfect mirror dramatically increases the graphene multilayer absorptivity as illustrated in Fig. 10. In the presence of the mirror, both overall absorptivity and narrow-band peak absorptivity are greatly

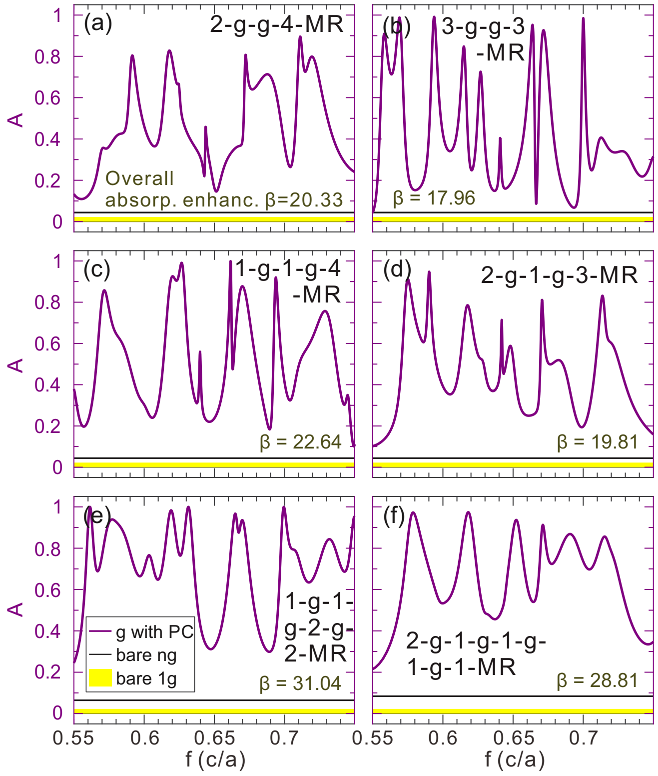

FIG. 10. Absorptivity spectra (solid purple lines) of multiple graphene layers embedded in the six-layer woodpile PC with perfect mirror beneath. For comparison, the free-standing bare monolayer graphene absorptivity (yellow filled color) and free-standing bare multilayer graphene absorptivity (solid black lines) are also plotted. The configurations of (a)–(f) differ from those of Fig. 9 only by the substrates.

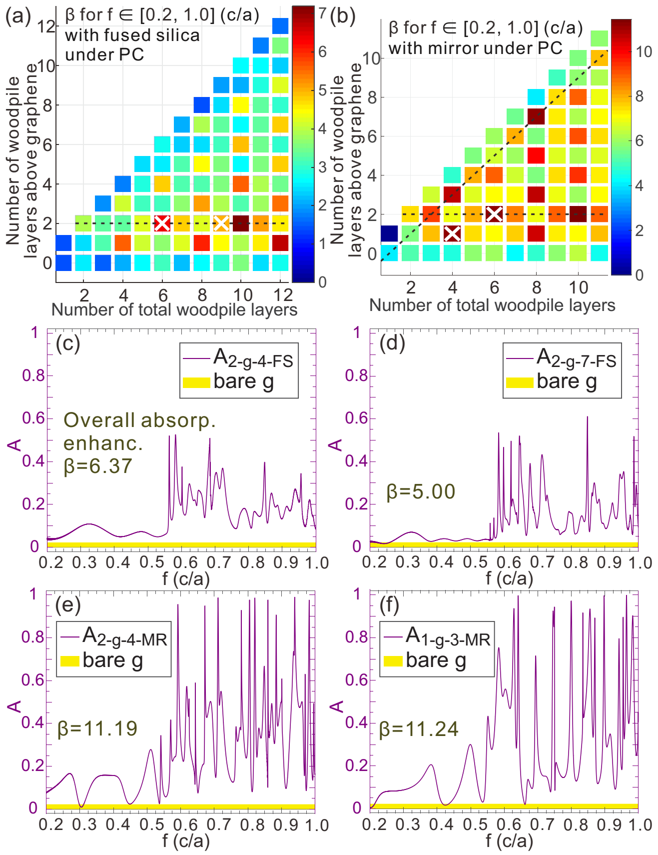

FIG. 11. Broadband absorptivity enhancements of graphene embedded in various configurations in various PCs. (a) and (b) Overall absorption enhancement in frequency range 0.20 to 1.00 c/a by placing a graphene monolayer at different locations within PCs with different number of woodpile layers, using (a) fused silica and (b) a perfect mirror as the substrate. The dashed lines mark the optimal locations for absorption enhancement. The white crosses indicate examples given in (c)–(f). (c) and (d) Absorptivity spectra of 2-g-4 and 2-g-7 configurations with substrate of fused silica. (e) and (f) Absorptivity spectra of 2-g-4 and 1-g-3 structures with perfect mirror substrate.

enhanced in the spectral range of interest. Remarkably, with three graphene layers distributed in the 1-g-1-g-2-g-2-MR architecture, the overall absorptivity reaches 69.6% as shown in Fig. 10(e).

Finally, we illustrate the very broadband nature of absorption enhancement by light trapping in the woodpile PC. In Figs. 11(a) and 11(b) we plot the overall absorptivity enhancement over the extensive frequency range from 0.2 to 1.0 c/a, in the two cases of substrate of fused silica and the perfect mirror. We give examples of configurations 2-g-4 and 2-g-7 with substrate of fused silica in Figs. 11(c) and 11(d). For the perfect mirror, we consider configurations 2-g-4 and 1-g-3 in Figs. 11(e) and 11(f). The overall absorptivity enhancements are 6.37, 5.00, 11.19, and 11.24, respectively. In these illustrations, the bandwidth to central frequency ratio is 1.33.

VI. CONCLUSION

In summary, we have demonstrated substantial and extensive enhancement of absorptivity in undoped graphene through light trapping in a simple-cubic woodpile photonic crystal. The existence of slow light, parallel-to-interface refraction modes, and other optical resonances greatly increases the graphene absorptivity and enhances light harvesting in a very broad bandwidth. The replacement of our undoped graphene sheets with doped layers may lead to further absorption enhancements. This would involve synergy between photonic crystal light trapping and plasmonic effects.

Our approach can be implemented in different frequency regimes by scaling the size of the photonic crystal or the refractive index contrast between the photonic crystal material and the background material. By taking advantage of a continuum of resonant modes, we achieve both broadband light harvesting and narrow-band near-unity light absorptivity. A distributed intercalation of graphene monolayers and bilayers collects different resonant modes in space.

Three-dimensional photonic crystals of various lattice symmetries have been fabricated through interference lithography [98] and layer-by-layer growth [99,100] in the infrared and visible regimes. A large-scale simple cubic woodpile photonic crystal made of TiO_2 with lattice constant 450 nm [86,101] has been shown to exhibit parallel-to-interface refractive modes light-trapping effects. The layer-by-layer growth method is amenable to the intercalation of single or multiple graphene monolayers and/or bilayers. For better support of graphene layer(s), a low refractive index material such as porous silica can replace the air fraction of the woodpile. This only weakly scales down the photonic bands frequencies while retaining the absorption features described in our TiO_2-air woodpile.

Ultrafast, broadband photodetectors with high responsivity are important for studying fast processes. Our method of broadband light-trapping enhancement of absorptivity may enhance the efficiencies of graphene and other two-dimensional-material-based optoelectronic devices.

ACKNOWLEDGMENTS

We are grateful to Professor Shawn Lin for stimulating discussions. This work was supported by the United States Department of Energy DOE-BES in a subcontract under Award DE-FG02-06ER46347.

---

[1] K. I. Bolotin, K. J. Sikes, Z. Jiang, M. Klima, G. Fudenberg, J. Hone, P. Kim, and H. L. Stormer, Solid State Commun. **146**, 351 (2008).
[2] K. S. Novoselov, A. K. Geim, S. V. Morozov, D. Jiang, Y. Zhang, S. V. Dubonos, I. V. Grigorieva, and A. A. Firsov, Science **306**, 666 (2004).
[3] Y. Zhang, Y.-W. Tan, H. L. Stormer, and P. Kim, Nature (London) **438**, 201 (2005).
[4] Z. Q. Li, E. A. Henriksen, Z. Jiang, Z. Hao, M. C. Martin, P. Kim, H. L. Stormer, and D. N. Basov, Nat. Phys. **4**, 532 (2008).
[5] R. R. Nair, P. Blake, A. N. Grigorenko, K. S. Novoselov, T. J. Booth, T. Stauber, N. M. R. Peres, and A. K. Geim, Science **320**, 1308 (2008).
[6] K. F. Mak, M. Y. Sfeir, Y. Wu, C. H. Lui, J. A. Misewich, and T. F. Heinz, Phys. Rev. Lett. **101**, 196405 (2008).
[7] A. A. Balandin, S. Ghosh, W. Bao, I. Calizo, D. Teweldebrhan, F. Miao, and C. N. Lau, Nano Lett. **8**, 902 (2008).
[8] C. Lee, X. Wei, J. W. Kysar, and J. Hone, Science **321**, 385 (2008).
[9] F. Bonaccorso, Z. Sun, T. Hasan, and A. C. Ferrari, Nat. Photon. **4**, 611 (2010).
[10] F. Xia, H. Wang, D. Xiao, M. Dubey, and A. Ramasubramaniam, Nat. Photon. **8**, 899 (2014).
[11] T. Wang and Y.-Q. Xu, Electronics **5**, 93 (2016).
[12] X. Li, L. Tao, Z. Chen, H. Fang, X. Li, X. Wang, J.-B. Xu, and H. Zhu, Appl. Phys. Rev. **4**, 021306 (2017).
[13] R.-J. Shiue, D. K. Efetov, G. Grosso, C. Peng, K. C. Fong, and D. Englund, Nanophotonics **6**, 1329 (2017).
[14] H. Zhang, Q. Bao, D. Tang, L. Zhao, and K. Loh, Appl. Phys. Lett. **95**, 141103 (2009).
[15] Z. Sun, T. Hasan, F. Torrisi, D. Popa, G. Privitera, F. Wang, F. Bonaccorso, D. M. Basko, and A. C. Ferrari, ACS Nano **4**, 803 (2010).
[16] M. Liu, X. B. Yin, E. Ulin-Avila, B. S. Geng, T. Zentgraf, L. Ju, F. Wang, and X. Zhang, Nature (London) **474**, 64 (2011).
[17] B. Sensale-Rodriguez, R. Yan, M. Zhu, D. Jena, L. Liu, and H. G. Xing, Appl. Phys. Lett. **101**, 261115 (2012).
[18] A. Majumdar, J. Kim, J. Vuckovic, and F. Wang, Nano Lett. **13**, 515 (2013).
[19] Z. Shi, L. Gan, T.-H. Xiao, H.-L. Guo, and Z.-Y. Li, ACS Photon. **2**, 1513 (2015).
[20] R. Yu, V. Pruneri, and F. J. García de Abajo, ACS Photon. **2**, 550 (2015).
[21] S. Bae, H. Kim, Y. Lee, X. Xu, J.-S. Park, Y. Zheng, J. Balakrishnan, T. Lei, H. Ri Kim, Y. I. Song, Y.-J. Kim, K. S. Kim, B. Özyilmaz, J.-H. Ahn, B. H. Hong, and S. Iijima, Nat. Nanotech. **5**, 574 (2010).
[22] N. Yang, J. Zhai, D. Wang, Y. Chen, and L. Jiang, ACS Nano **4**, 887 (2010).
[23] Y. Song, X. Li, C. Mackin, X. Zhang, W. Fang, T. Palacios, H. Zhu, and J. Kong, Nano Lett. **15**, 2104 (2015).
[24] F. Xia, T. Mueller, Y.-m. Lin, A. Valdes-Garcia, and P. Avouris, Nat. Nanotech. **4**, 839 (2009).
[25] T. Mueller, F. Xia, and P. Avouris, Nat. Photon. **4**, 297 (2010).
[26] Y. Liu, R. Cheng, L. Liao, H. Zhou, J. Bai, G. Liu, L. Liu, Y. Huang, and X. Duan, Nat. Commun. **2**, 579 (2011).
[27] B. Y. Zhang, T. Liu, B. Meng, X. Li, G. Liang, X. Hu, and Q. J. Wang, Nat. Commun. **4**, 1811 (2013).
[28] X. Gan, R.-J. Shiue, Y. Gao, I. Meric, T. F. Heinz, K. Shepard, J. Hone, S. Assefa, and D. Englund, Nat. Photon. **7**, 883 (2013).
[29] C.-H. Liu, Y.-C. Chang, T. B. Norris, and Z. Zhong, Nat. Nanotech. **9**, 273 (2014).
[30] Z. Sun and H. Chang, ACS Nano **8**, 4133 (2014).
[31] F. H. L. Koppens, T. Mueller, P. Avouris, A. C. Ferrari, M. S. Vitiello, and M. Polini, Nat. Nanotech. **9**, 780 (2014).
[32] J. M. Dawlaty, S. Shivaraman, M. Chandrashekhar, F. Rana, and M. G. Spencer, Appl. Phys. Lett. **92**, 042116 (2008).
[33] F. Xia, T. Mueller, R. Golizadeh-Mojarad, M. Freitag, Y.-m. Lin, J. Tsang, V. Perebeinos, and P. Avouris, Nano Lett. **9**, 1039 (2009).
[34] T. J. Echtermeyer, L. Britnell, P. K. Jasnos, A. Lombardo, R. V. Gorbachev, A. N. Grigorenko, A. K. Geim, A. C. Ferrari, and K. S. Novoselov, Nat. Commun. **2**, 458 (2011).
[35] Z. Fang, Z. Liu, Y. Wang, P. M. Ajayan, P. Nordlander, and N. J. Halas, Nano Lett. **12**, 3808 (2012).
[36] S. Song, Q. Chen, L. Jin, and F. Sun, Nanoscale **5**, 9615 (2013).
[37] Y. Cai, J. Zhu, and Q. H. Liu, Appl. Phys. Lett. **106**, 043105 (2015).
[38] F. Xiong, J. Zhang, Z. Zhu, X. Yuan, and S. Qin, Sci. Rep. **5**, 16998 (2015).
[39] Z. Fang, Y. Wang, Z. Liu, A. Schlather, P. M. Ajayan, F. H. L. Koppens, P. Nordlander, and N. J. Halas, ACS Nano **6**, 10222 (2012).
[40] M. Jablan, H. Buljan, and M. Soljačić, Phys. Rev. B **80**, 245435 (2009).
[41] S. Thongrattanasiri, F. H. L. Koppens, and F. J. García de Abajo, Phys. Rev. Lett. **108**, 047401 (2012).
[42] A. Y. Nikitin, F. Guinea, F. J. Garcia-Vidal, and L. Martin-Moreno, Phys. Rev. B **85**, 081405 (2012).
[43] A. Andryieuski and A. V. Lavrinenko, Opt. Express **21**, 9144 (2013).

[44] Z. Fang, Y. Wang, A. E. Schlather, Z. Liu, P. M. Ajayan, F. J. García de Abajo, P. Nordlander, X. Zhu, and N. J. Halas, Nano Lett. **14**, 299 (2014).
[45] S. Ke, B. Wang, H. Huang, H. Long, K. Wang, and P. Lu, Opt. Express **23**, 8888 (2015).
[46] S. Xiao, T. Wang, Y. Liu, C. Xu, X. Han, and X. Yan, Phys. Chem. Chem. Phys. **18**, 26661 (2016).
[47] W. Gao, J. Shu, C. Qiu, and Q. Xu, ACS Nano **6**, 7806 (2012).
[48] X. Zhu, W. Yan, P. Uhd Jepsen, O. Hansen, N. Asger Mortensen, and S. Xiao, Appl. Phys. Lett. **102**, 131101 (2013).
[49] T. R. Zhan, F. Y. Zhao, X. H. Hu, X. H. Liu, and J. Zi, Phys. Rev. B **86**, 165416 (2012).
[50] L. Tang, J. Du, C. Du, P. Zhu, and H. Shi, Opt. Express **22**, 20214 (2014).
[51] L. Tang, H. Shi, J. Yang, C. Du, F. Gao, J. Zhu, and J. Du, Microelectron. Eng. **145**, 58 (2015).
[52] Z. Wang and Y. Hou, Opt. Express **25**, 19185 (2017).
[53] X. Wang, Z. Cheng, K. Xu, H. K. Tsang, and J.-B. Xu, Nat. Photon. **7**, 888 (2013).
[54] A. Pospischil, M. Humer, M. M. Furchi, D. Bachmann, R. Guider, T. Fromherz, and T. Mueller, Nat. Photon. **7**, 892 (2013).
[55] H. Liu, S. Zha, P. Liu, X. Zhou, and L.-a. Bian, Superlattices Microstruct. **117**, 429 (2018).
[56] M. Furchi, A. Urich, A. Pospischil, G. Lilley, K. Unterrainer, H. Detz, P. Klang, A. M. Andrews, W. Schrenk, G. Strasser, and T. Mueller, Nano Lett. **12**, 2773 (2012).
[57] X. Gan, K. F. Mak, Y. Gao, Y. You, F. Hatami, J. Hone, T. F. Heinz, and D. Englund, Nano Lett. **12**, 5626 (2012).
[58] R.-J. Shiue, X. Gan, Y. Gao, L. Li, X. Yao, A. Szep, D. Walker, Jr., J. Hone, and D. Englund, Appl. Phys. Lett. **103**, 241109 (2013).
[59] C.-C. Guo, Z.-H. Zhu, X.-D. Yuan, W.-M. Ye, K. Liu, J.-F. Zhang, W. Xu, and S.-Q. Qin, Adv. Opt. Mater. **4**, 1955 (2016).
[60] M. Grande, M. A. Vincenti, T. Stomeo, G. V. Bianco, D. de Ceglia, N. Aközbek, V. Petruzzelli, G. Bruno, M. De Vittorio, M. Scalora, and A. D'Orazio, Opt. Express **22**, 31511 (2014).
[61] G. Zheng, H. Zhang, L. Xu, and Y. Liu, Opt. Lett. **41**, 2274 (2016).
[62] G. Zheng, H. Zhang, and L. Bu, Plasmonics **12**, 271 (2017).
[63] R. Wang, T. Sang, L. Wang, J. Gao, Y. Wang, and J. Wang, Optik **157**, 651 (2018).
[64] F. Liu, L. Chen, Q. Guo, J. Chen, X. Zhao, and W. Shi, Opt. Express **23**, 21097 (2015).
[65] B. Zhao, J. M. Zhao, and Z. M. Zhang, Appl. Phys. Lett. **105**, 031905 (2014).
[66] B. Zhao, J. M. Zhao, and Z. M. Zhang, J. Opt. Soc. Am. B **32**, 1176 (2015).
[67] L. Zhang, L. Tang, W. Wei, X. Cheng, W. Wang, and H. Zhang, Opt. Express **24**, 20002 (2016).
[68] G. Pirruccio, L. Martín Moreno, G. Lozano, and J. Gómez Rivas, ACS Nano **7**, 4810 (2013).
[69] W. Zhao, K. Shi, and Z. Lu, Opt. Lett. **38**, 4342 (2013).
[70] K. Shi, R. R. Haque, L.-F. Mao, and Z. Lu, Opt. Commun. **339**, 47 (2015).
[71] S. John, Phys. Rev. Lett. **58**, 2486 (1987).
[72] J.-T. Liu, N.-H. Liu, J. Li, X. J. Li, and J.-H. Huang, Appl. Phys. Lett. **101**, 052104 (2012).
[73] M. Grande, M. A. Vincenti, T. Stomeo, D. d. Ceglia, V. Petruzzelli, M. D. Vittorio, M. Scalora, and A. D'Orazio, IEEE Photon. J. **6**, 1 (2014).
[74] Y. Long, L. Shen, H. Xu, H. Deng, and Y. Li, Sci. Rep. **6**, 32312 (2016).
[75] L. Yang, J. Wang, and C. Lu, Optik **158**, 508 (2018).
[76] J. R. Piper and S. Fan, ACS Photon. **1**, 347 (2014).
[77] Y. Liu, A. Chadha, D. Zhao, J. R. Piper, Y. Jia, Y. Shuai, L. Menon, H. Yang, Z. Ma, S. Fan, F. Xia, and W. Zhou, Appl. Phys. Lett. **105**, 181105 (2014).
[78] S. Fan and J. D. Joannopoulos, Phys. Rev. B **65**, 235112 (2002).
[79] A. Chutinan and S. John, Phys. Rev. A **78**, 023825 (2008).
[80] H. Tang, K. Prasad, R. Sanjinès, P. E. Schmid, and F. Lévy, J. Appl. Phys. **75**, 2042 (1994).
[81] A. Amtout and R. Leonelli, Phys. Rev. B **51**, 6842 (1995).
[82] N. Hosaka, T. Sekiya, C. Satoko, and S. Kurita, J. Phys. Soc. Jpn. **66**, 877 (1997).
[83] G. Demésy and S. John, J. Appl. Phys. **112**, 074326 (2012).
[84] S. Foster and S. John, Energy Environ. Sci. **6**, 2972 (2013).
[85] P. Kuang, A. Deinega, M.-L. Hsieh, S. John, and S.-Y. Lin, Opt. Lett. **38**, 4200 (2013).
[86] B. J. Frey, P. Kuang, M.-L. Hsieh, J.-H. Jiang, S. John, and S.-Y. Lin, Sci. Rep. **7**, 4171 (2017).
[87] D. S. L. Abergel, V. Apalkov, J. Berashevich, K. Ziegler, and T. Chakraborty, Adv. Phys. **59**, 261 (2010).
[88] T. Ando, A. Kanda, K. Wakabayashi, A. Konishi, T. Kubo, and T. Enoki, *Physics and Chemistry of Graphene: Graphene to Nanographene*, edited by T. Enoki and T. Ando (CRC Press Taylor & Francis Group, Boca Raton, FL, 2014).
[89] K. Ziegler, Phys. Rev. Lett. **97**, 266802 (2006).
[90] A. H. Castro Neto, F. Guinea, N. M. R. Peres, K. S. Novoselov, and A. K. Geim, Rev. Mod. Phys. **81**, 109 (2009).
[91] T. Stauber, N. M. R. Peres, and A. K. Geim, Phys. Rev. B **78**, 085432 (2008).
[92] A. F. Oskooi, D. Roundy, M. Ibanescu, P. Bermel, J. D. Joannopoulos, and S. G. Johnson, Comput. Phys. Commun. **181**, 687 (2010).
[93] A. Taflove, S. G. Johnson, and A. Oskooi, *Advances in FDTD Computational Electrodynamics: Photonics and Nanotechnology* (Artech House, Norwood, MA, 2013).
[94] F. Wang, Y. Zhang, C. Tian, C. Girit, A. Zettl, M. Crommie, and Y. R. Shen, Science **320**, 206 (2008).
[95] J. Nilsson, A. H. Castro Neto, F. Guinea, and N. M. R. Peres, Phys. Rev. Lett. **97**, 266801 (2006).
[96] T. Ohta, A. Bostwick, T. Seyller, K. Horn, and E. Rotenberg, Science **313**, 951 (2006).
[97] D. S. L. Abergel and V. I. Fal'ko, Phys. Rev. B **75**, 155430 (2007).
[98] M. Campbell, D. N. Sharp, M. T. Harrison, R. G. Denning, and A. J. Turberfield, Nature (London) **404**, 53 (2000).
[99] S. Y. Lin, J. G. Fleming, D. L. Hetherington, B. K. Smith, R. Biswas, K. M. Ho, M. M. Sigalas, W. Zubrzycki, S. R. Kurtz, and J. Bur, Nature (London) **394**, 251 (1998).
[100] S.-Y. Lin, J. G. Fleming, R. Lin, M. M. Sigalas, R. Biswas, and K. M. Ho, J. Opt. Soc. Am. B **18**, 32 (2001).
[101] B. J. Frey, P. Kuang, S.-Y. Lin, J.-H. Jiang, and S. John, J. Vac. Sci. Technol. B **33**, 021804 (2015).